

APOSR-TR- 82-0547

12



UNIVERSITY OF MINNESOTA

ACOUSTIC STRAIN VISUALIZATION IN
STRUCTURAL MATERIALS

by

Rolf K. Mueller

AD A116992

DTIC FILE COPY

DTIC
ELECTE
JUL 19 1982
H

Approved for public release/
distribution unlimited.

82 07 19 081

UNCLASSIFIED

SECURITY CLASSIFICATION OF THIS PAGE (When Data Entered)

REPORT DOCUMENTATION PAGE		READ INSTRUCTIONS BEFORE COMPLETING FORM
1. REPORT NUMBER AFOSR-TR- 82-0547	2. GOVT ACCESSION NO. AD-A116 992	3. RECIPIENT'S CATALOG NUMBER
4. TITLE (and Subtitle) ACOUSTIC STRAIN VISUALIZATION IN STRUCTURAL MATERIALS		5. TYPE OF REPORT & PERIOD COVERED FINAL REPORT Sept 80 thur Mar 82
		6. PERFORMING ORG. REPORT NUMBER
7. AUTHOR(s) Rolf K. Mueller		8. CONTRACT OR GRANT NUMBER(s) F49620-80-C-0102
9. PERFORMING ORGANIZATION NAME AND ADDRESS Department of Electrical Engineering University of Minnesota Minneapolis, MN 55455		10. PROGRAM ELEMENT, PROJECT, TASK AREA & WORK UNIT NUMBERS 61102F 4049/00
11. CONTROLLING OFFICE NAME AND ADDRESS AFOSR / NE Bolling AFB, Bldg #410 Washington, DC 20332		12. REPORT DATE 1982
		13. NUMBER OF PAGES 48
14. MONITORING AGENCY NAME & ADDRESS (if different from Controlling Office)		15. SECURITY CLASS. (of this report) UNCLASSIFIED
		15a. DECLASSIFICATION/DOWNGRADING SCHEDULE
16. DISTRIBUTION STATEMENT (of this Report) Approved for public release; distribution unlimited.		
17. DISTRIBUTION STATEMENT (of the abstract entered in Block 20, if different from Report)		
18. SUPPLEMENTARY NOTES		
19. KEY WORDS (Continue on reverse side if necessary and identify by block number) Acoustic Tomography, Time of Flight, Acoustic Velocity		
20. ABSTRACT (Continue on reverse side if necessary and identify by block number) An experimental acousto-optic time of flight measurement system has been designed and built. In this system an acoustic pulse is launched through a material and the time of transit is measured by optical observation of the arrival time. A timing accuracy of plus or minus 80 P Sec was demonstrated which is 50 times more sensitive than that required to indicate residual stresses in steel on the order of 1,000 PSI. Unfortunately, experimental difficulties precluded the measurement of residual stresses in the test piece.		

Acoustic strain visualization in structural materials

Final Report

Sponsored by

Advanced Research Projects Agency (DOD)
ARPA Order No. 4049
monitored by AFOSR under Contract #F49620-80-C-0102

Principal Investigator

R. K. Mueller
Department of Electrical Engineering
University of Minnesota
Minneapolis, Minnesota 55455

DTIC
ELECTE
JUL 19 1982
H

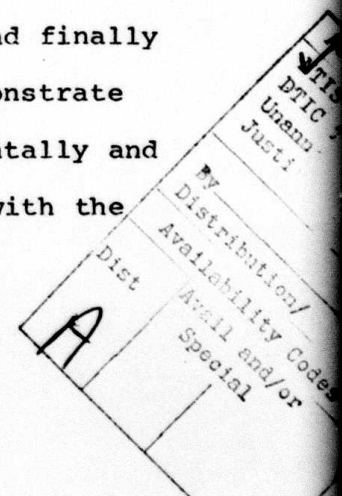
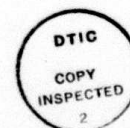
AIR FORCE OFFICE OF SCIENTIFIC RESEARCH (AFSC)
NOTICE OF TRANSMITTAL TO DTIC
This technical report has been reviewed and is
approved for public release IAW AFR 190-12.
Distribution is unlimited.
MATTHEW J. KERPER
Chief, Technical Information Division

The views and conclusions contained in this document are those of the author and should not be interpreted as necessarily representing the official policies, either expressed or implied, of the Defense Advanced Research Projects Agency or the U.S. government.

Introduction and Summary

The possibility of stress field visualizations by acoustic time of flight tomography has been discussed in the literature by several authors [1-3]. In these attempts the sound is coupled to the test object via a water bath which poses severe limitations to the practical applicability of this otherwise very promising approach to stress field visualization. The alternative more versatile approach considered here is to use optical (laser) means to generate an acoustic excitation on the work piece and to read out the acoustic signal after it traversed the test object optically by a receiving laser beam. The possibility of laser excitation has been shown in the literature, [4] as has the possibility of acoustic laser read out [5,6]. The specific objective of the work reported here was to demonstrate that a laser read out system with the sensitivity and accuracy required for stress visualization by longitudinal acoustic waves can be built and operated.

In Section one of this report we describe the main components of the time of flight measurement system built under this contract. In section 2 the electronic circuitry which controls and connects these subsystems is described. In section three the time measurement accuracy of the system is analyzed and finally in section 4 some experiments are described which demonstrate that the expected accuracy has been achieved experimentally and that stress induced velocity changes can be observed with the system.



Section 1.

The principle of operations of the time of flight measurement system is illustrated in Fig. 1. The acoustic pulse is launched into the test sample via a piezoelectric transducer driven by a pulse generator. The acoustic pulse after traversing the sample is detected by a laser beam reflected from the sample. The detection is based on the fact that the reflected laser beam suffers a phase modulation by the arriving of the acoustic pulse. This phase modulation is transformed into an amplitude modulation by the optical interferometer and transformed into an electrical signal by a photoreceiver. This electrical signal is fed into an interval timer which is activated by the pulse generator as it launches the acoustic pulse into the sample. The lapse time is then recorded by this interval timer. An oscilloscope triggered by the pulse generator displays the initial and received pulses.

The major components of this system are:

- 1) a mechanical stage which accomodates the test sample and the optical receiver.
- 2) The laser source.
- 3) The acoustic excitation sub-system.
- 4) The optical interferometer and receiver subsystem.
- 5) The interval timer and control electronics.

The mechanical stage.

The mechanical stage, because of the high resolution requirement, has to be very stable, to minimize environmental acoustic noise and vibrations. A schematic of the stage is shown in Fig. 2. The sample stage and a platform supporting the optical system are mounted on a heavy, rail-type lathe bed. The

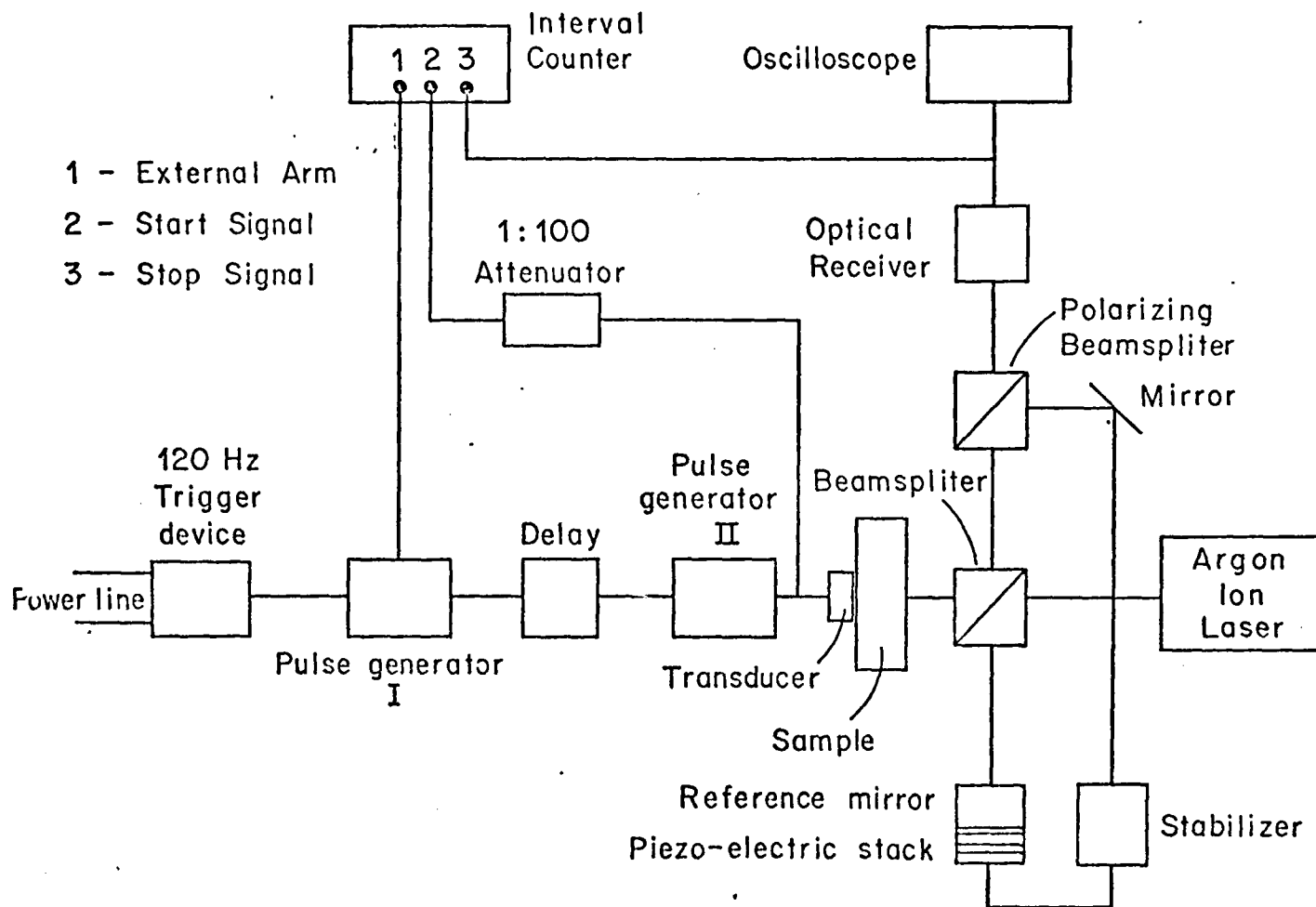


Fig. 1 Schematic of time of flight measurement system.

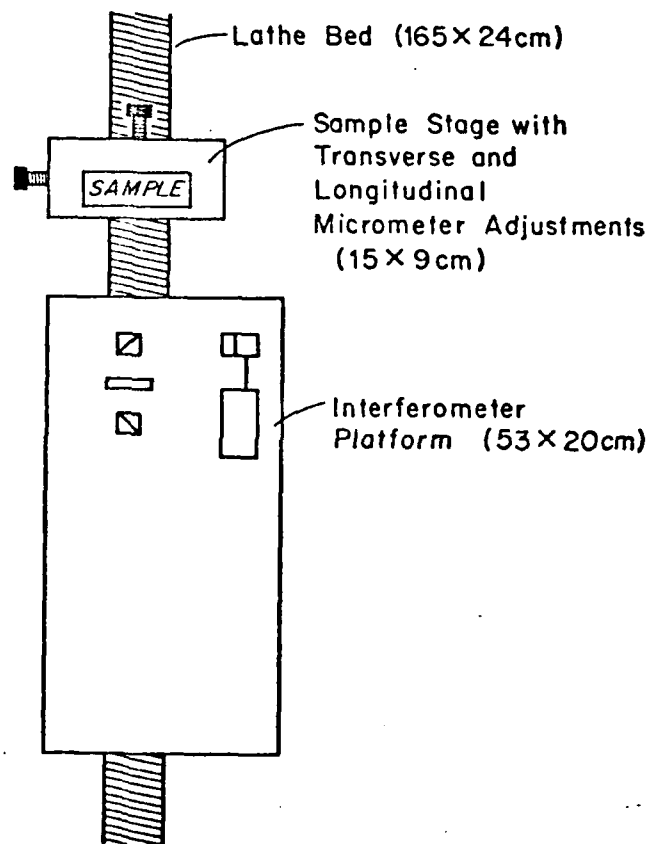


Fig. 2 Schematic of mechanical stage.

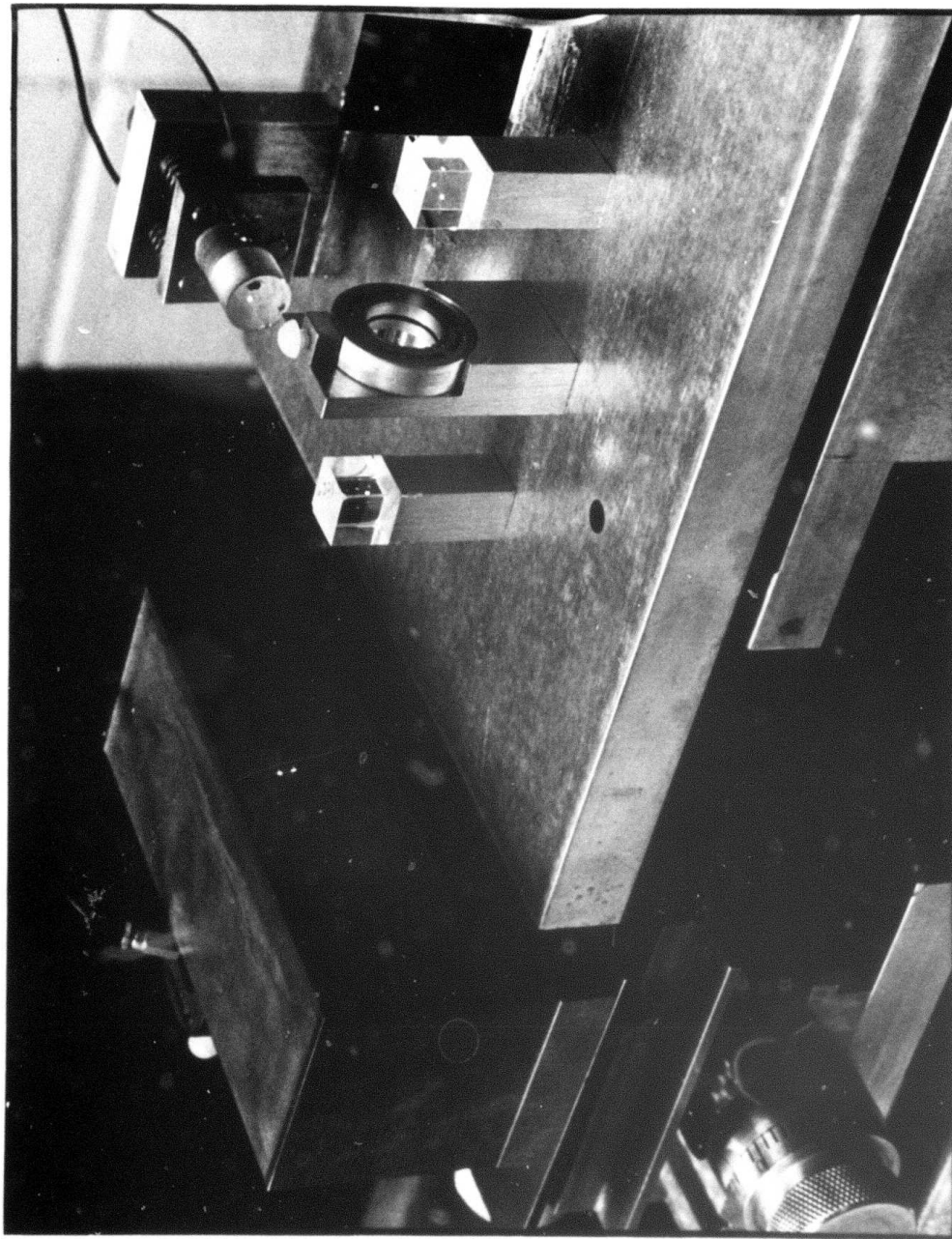


Figure 3 : Mechanical stage with interferometer assembly.

foundation of the interferometer platform is a rectangular steel box. The $3/4$ " thick steel platform itself rests on top of a $1/2$ " rubber damping pad. Four corner bolts allow for leveling adjustments of platform placement.

The sample stage, supported also on the lathe bed, has been designed with a view toward maximizing flexibility in both translational and rotational movements. Translational movements, both longitudinal and transverse, are controlled through micrometers. The sample itself is capable of being rotated horizontally. In addition, a set screw on the stage itself makes it possible to tilt the sample with respect to the optical axis of the interferometer. An actual view of the mechanical stage is given in Fig. 3.

The laser source

The laser source used in the optical system is a Spectro physics argon ion laser model #164 equipped with an etalon assembly to insure single frequency operation. Single frequency operation results in a long "coherence length". The long coherence length permits interferometric measurements with an interferometer of widely differing path length in the two interferometer arms. This feature removes restrictions in the interferometer design which are especially important for any practical realizations of the time of flight measurement system discussed in this report.

In the originally proposed design concept a single frequency HeNe laser Tropel Mod #130 was considered, and used in the first version of the interferometric measurement systems. Experiments with this system however showed that the output power of this

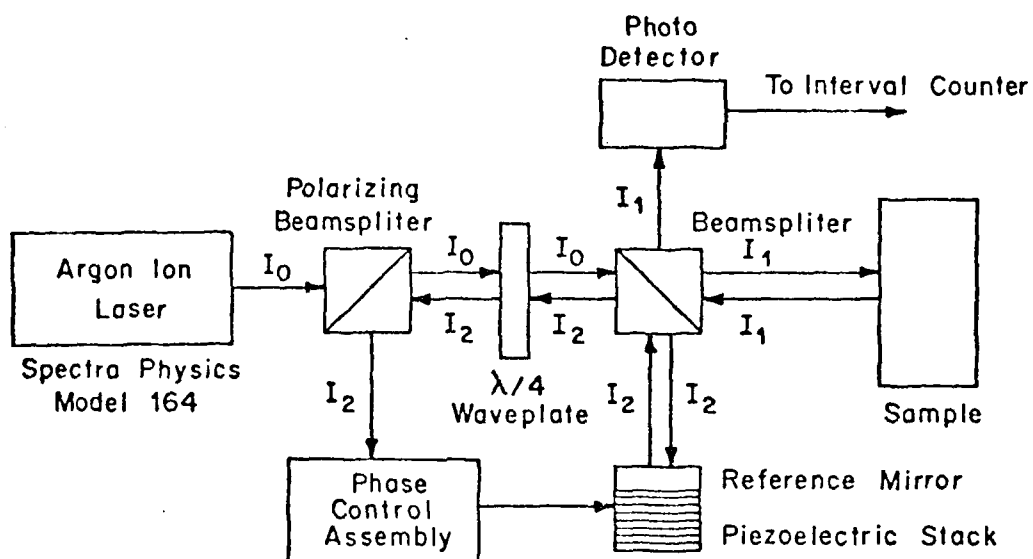


Fig. 4 Schematic of interferometer assembly.

laser was insufficient to obtain the required signal to noise ratio in the optical output signal. The system was consequently redesigned around the more powerful argon ion laser.

The interferometer

A schematic of the interferometer assembly is shown in Fig. 4. The linearly polarized laser beam I_0 enters the interferometer assembly through a polarizing beam splitter B_1 . A polarizing beam splitter completely transmits an appropriately polarized beam, and completely reflects it if the polarization is rotated by 90 degrees. The transmitted beam I_0 passes through a $\lambda/4$ plate. A $\lambda/4$ plate appropriately oriented transforms linearly polarized light into circularly polarized light. After traversing the $\lambda/4$ plate the beam enters the 50/50 Beam splitter B_2 , which constitutes together with the test sample and the reference mirror, a Michelson interferometer. In the Beam splitter B_2 the incident beam I_0 is decomposed into two partial beams I_{01} and I_{02} of equal intensity which propagate along the two interferometer arms.

The measurement arm of the interferometer is terminated by the test sample which reflects the beam I_{01} back to the beam splitter. The reference arm of the interferometer, along which the beam I_{02} propagates, is terminated by a reference mirror mounted on a piezoelectric stack. The path length of this arm can be varied over several wavelength by activating the piezoelectric stack via a feedback control loop. The reflected beams I_{01} and I_{02} are recombined in the beamsplitter B_2 and partitioned into the two interferometer output beams I_1 and I_2 . The

interferometer output beam I_1 is intercepted by a photodetector assembly which senses the intensity variations in this beam. The second interferometer output beam I_2 is travelling back to the $\lambda/4$ plate, which transforms the circularly polarized light back into linearly polarized light. Since reflection reverses the sense of rotation in circularly polarized light, and since all components of the interferometer output beams have suffered an odd number of reflections the sense of rotation in I_2 has been reversed, relative to the incoming beam I_0 . Traversing the $\lambda/4$ plate this opposite circular polarization is transformed into a linear polarization orthogonal to that of I_0 . The polarizing beam splitter B_1 therefore totally reflects the output beam I_2 into the photodetector of the phase control assembly. This closes the phase control loop, and isolates the laser from the interferometer. The objective of the phase control loop is to establish and maintain equal intensity in the interferometer output beams I_1 and I_2 against low frequency disturbances in the path length of the two interferometer arms, caused by mechanical vibrations of the system, air turbulence and other environmental disturbances.

The acoustic excitation system.

As mentioned in the introduction the acoustic signal is launched into the test sample by a piezoelectric transducer. Since the test samples, described in detail later, were made of steel, we designed and fabricated a magnetic transducer holder shown in Fig. 5 which allowed to attach the transducer securely to the sample but made it easy to slide the transducer assembly

over the sample surface. A thin film of glycerol was used as coupling medium. The transducers proper were 4x4 and 8x8 mm square ceramic transducers with a nominal frequencies of 7 MHz and 5 MHz supplied by Channel Industries in Sta. Barbara. The transducers were excited with a narrow 40 nsec pulse of 400 to 600 volts provided by a Velonex Mod 350 pulse generator, which was triggered by the control electronics to be described later. Since the transducers were essentially air backed the narrow pulse excitation gave rise to an acoustic pulse, which was essentially a damped sinusoidal pulse with a ringing frequency of 3.95 and 3.2 MHz for the two transducers respectively.

The travel time of the pulse through the sample was measured with a Hewlit Packard interval timer Mod #5370A which not only measured the pulse time of flight but also computed the mean and standard deviation for pulse sequences.

Section 2

The subsystems described in the previous sections were connected by electronic control circuitry which are described in this section.

The interferometer stabilizer.

The objective of the interferometer shown in Fig. 4 and briefly described above is to transform the small phase modulation which the laser beam suffers as it is reflected from the acoustically excited sample surface, into intensity modulation.

As described earlier the intensities of the two beams I_{01} and I_{02} coming from the two arms of the interferometer are equal:

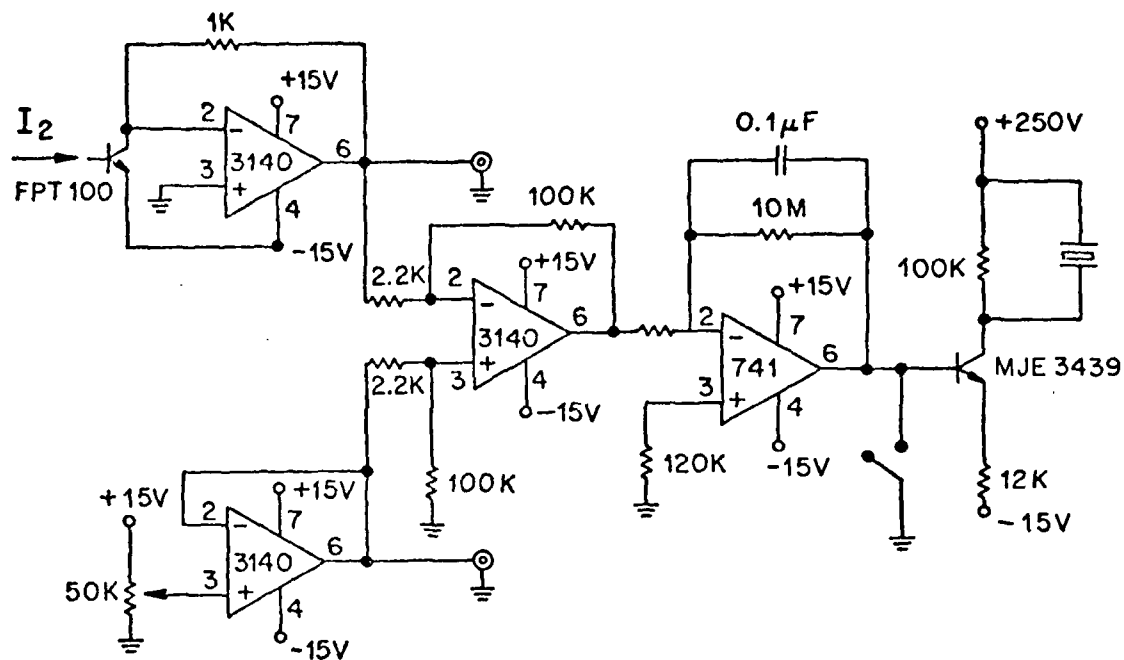


Fig. 6 Schematic of interferometer stabilizer.

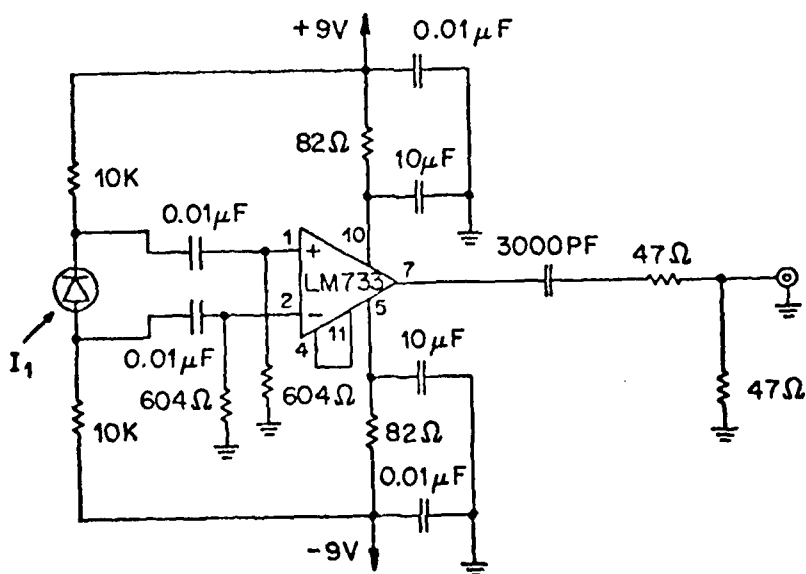


Fig. 7 Schematic of photoreceiver.

$I_{01} = I_{02} = \frac{I_0}{2}$. They are recombined in the beamsplitter B_2 to form the two interferometer output beams I_1 and I_2 . The recombination and repartitioning at the beamsplitter depends on the relative phases of the beams I_{01} and I_{02} . Letting the complex amplitudes A_{01} of I_{01} and A_{02} of I_{02} :

$$A_{01} = \sqrt{I_{01}} = \sqrt{I_0/2}, \quad A_{02} = \sqrt{I_{02}} \cdot e^{i\phi} = \sqrt{I_0/2} e^{i\phi} \quad (1)$$

where ϕ is the relative phase of the two beams at the beamsplitter. Realizing that reflection on the beamsplitter changes the phase by 90° whereas transmission does not affect the phase we find for the two output beam intensities:

$$\begin{aligned} I_1 &= \frac{I_0}{4} |i + e^{i\tau}|^2 = \frac{I_0}{2} (1 - \sin\phi) \\ I_2 &= \frac{I_0}{4} |1 + ie^{i\tau}|^2 = \frac{I_0}{2} (1 + \sin\phi) \end{aligned} \quad (2)$$

Assuming for the moment that the two arms of the interferometer are absolutely stable and the beam I_{01} suffers a small phase - disturbance δ due to the presence of an acoustic excitation on the sample surface we obtain for its effect on the intensity of the output beam I_1 :

$$I_1 = \frac{I_0}{2} (1 - \sin\phi \cos\delta + \cos\phi \sin\delta) \quad (3)$$

or because of the smallness of δ :

$$I_1 = \frac{I_0}{2} (1 - \sin\phi + \delta \cos\phi) \quad (4)$$

Obviously the intensity fluctuation in the output beam caused by the acoustic disturbance is maximized for $\phi = 0$, that is for the

case that both beams I_{01} and I_{02} arrive in phase at the beamsplitter. With no acoustic excitation present this condition implies that the two output beams I_1 and I_2 of the interferometer are of equal intensity. Due to unavoidable environmental disturbances such a balance can not be maintained without external stabilization. There are a large number of environmental effects which tend to offset the interferometer balance, e.g. temperature changes, which affect the optical pathlength, air turbulence in the optical path, building vibrations and acoustic noise in the environment. One common characteristic of these disturbances is that they are of relatively low frequency compared to the frequency of the signal of interest, and their effect on the system decreases rapidly with increasing frequency. Their effect can therefore be eliminated by stabilizing the interferometer against low frequency disturbances at the proper operating point of zero phase difference and then to remove the remaining small low and medium frequency disturbances by appropriate high pass filtering of the optical detector output. The low frequency stabilization is effected by a piezoelectric stack which carries the reference mirror of the interferometer and which when activated can change the path length of the reference arm of the interferometer over several optical wave length. This stack is activated by a control circuit shown in Fig. 6 which measures the intensity of the interferometer output beam I_2 and compares it with an internal reference. If the intensity of I_2 deviates from the internal reference a difference signal appears at the input of the first operational amplifier. This signal is amplified, low pass

filtered, and applied to the base of a high voltage transistor, which drives the stack to a new quiescent position. The total voltage swing is ± 120 volts which allows the stack to follow apparent path-length changes of about $\pm 2\lambda$ (λ is the optical wavelength of the laser beam.) This is sufficient to compensate for the most severe low frequency disturbances. For the rare case that the regulator runs against its limit, a reset button is provided which grounds the base of the high voltage transistor and thereby puts the stack voltage back into the center of the regulating range.

Experiments with this control system showed that a bandwidth of about 100 Hz was sufficient to suppress environmental phase disturbances to a level which could be handled by high pass filtering of the optical receiver output. Attempts to widen the bandwidth of the controller tended to cause internal oscillations. The low frequency response of the controller makes it completely insensitive to the high frequency (2 to 10 MHz) of the acoustic signal of interest. With the control loop in place the intensity fluctuations in the interferometer output beam caused by the environment were reduced to the order of several percent. The corresponding residual phase jitter $\Delta\phi$ is therefore about $\pi/100$. This residual phase jitter is still about one to two orders of magnitude larger than the desired acoustically generated phase excursion δ . However since the phase jitter $\Delta\phi$ is of much lower frequency (~ 2 KHz) than the desired acoustic signal δ (~ 2 MHz) it can be completely removed by high pass filtering of the output of the optical receiver. Since the residual phase

jitter is very small compared to 1 radian we can rewrite the interferometer output intensity I_1 derived above in eq. (3) as

$$I_1 = \frac{I_0}{2} (1 - \Delta\phi + \delta) \quad (5)$$

by neglecting higher than first order terms in $\Delta\phi$. From this intensity, the photoreceiver to be described next, derives an estimate of the acoustic signal δ .

The photo receiver.

The photo receiver consists of an optical sensor followed by an amplifier. (see Fig. 7) The optical sensor is a high speed Hewlett Packard photo diode H.P. 4220. followed by a low noise operational amplifier. The design objectives were: shot noise limited operation, an effective bandwidth of 10 MHz and an output peak voltage of $> .2$ Volts over the 50Ω load required by the interval timer.

The photo diode has a nominal capacitance of 2 pF. which should allow one to operate the diode into an effective load of $10 K\Omega$ and still achieve the design goal of 10 MHz frequency response. However parasitic capacitances of about 20 pF. in the assembled amplifier circuit, which we could not eliminate made it necessary to reduce the effective photo diode load resistor R to $1K\Omega$. The requirement to achieve shot noise limited operation with this reduced load resistor, put as will be shown below, a power requirement of at least 10 mW on the laser source. This is a factor ten higher than the power which was available from the originally planned Tropel laser. This increased power

requirement made it necessary to redesign the interferometer system to operate with an Argon Ion laser which gave sufficient power to obtain shot noise limited operation.

The laser power requirement is determined by the following consideration: The apparent noise voltage at the amplifier input with a noise figure q is given by:

$$V_n = q V_{\text{therm}} + V_{\text{shot}} \quad (6)$$

where V_{therm} is the thermal noise of the input resistor R :

$$V_{\text{therm}} = \sqrt{2kTB} \quad (7)$$

and V_{shot} the shot noise voltage generated over the same resistor by the dc component of the photodiode output current $i = \eta I_1$:

$$V_{\text{shot}} = R \cdot \sqrt{\eta I_1 e B} \quad (8)$$

where k is the Boltzmann constant, T the temperature in $^{\circ}\text{K}$, B the required bandwidth of 10 MHz, η the photodiode efficiency $\eta = .3$ Amp/Watt, and e the electronic charge.

Defining (more or less arbitrarily) as condition for shot noise limited operations a ratio γ between shot noise voltage V_{shot} and amplifier noise voltage $q V_{\text{therm}}$ of

$$\gamma = \frac{V_{\text{shot}}}{q V_{\text{therm}}} > 3 \quad (9)$$

one obtain for the required power in the interferometer output beam I_1 impinging on the photodiode:

$$I_1 > 18 \frac{q^2 k T}{e \eta R} \text{ [Watt]} \quad (10)$$

With a noise figure of $q = 2$ one obtains from eq. (9)

$$I_1 > 2.25 \text{ [m Watts]}. \quad (11)$$

Assuming a 50% transmission loss in the optical system this leads to a required laser power of about 10 m W.

In order to obtain with the excitation scheme described above a signal pulse in the range of 200 to 800 mV an amplification factor of 100 was required. This amplification and the required high pass filtering was achieved with the single stage amplifier shown in Fig. 5. The noise output voltage was 3.5 mV rms which agreed well with the calculated shot noise output, indicating that no other noise sources were present. The resulting signal to noise ratio ranged from 24 to 36 DB. As we show later this noise is the major factor limiting the accuracy of the acoustic transit time measurement.

The timing control.

The objective of the timing control is to set the repetition rate for the transit time measurement, provide an arming and hold pulse, and appropriate starting and stop signals to the interval timer. A block diagram of the timing control is shown in Fig. 8.

The repetition rate of the time of flight measurement sequence has to be slow enough to allow the acoustic excitation in the test sample to decay below the noise level before the next acoustic pulse is launched into the test object. Because of the low acoustic attenuation in steel, reverberation above noise-level persist in the test object for about 20 times the pulse transit time of 8.7 μ sec. These reverberations limit the acceptable pulse repetition rate to about 5 KHz. It was found however

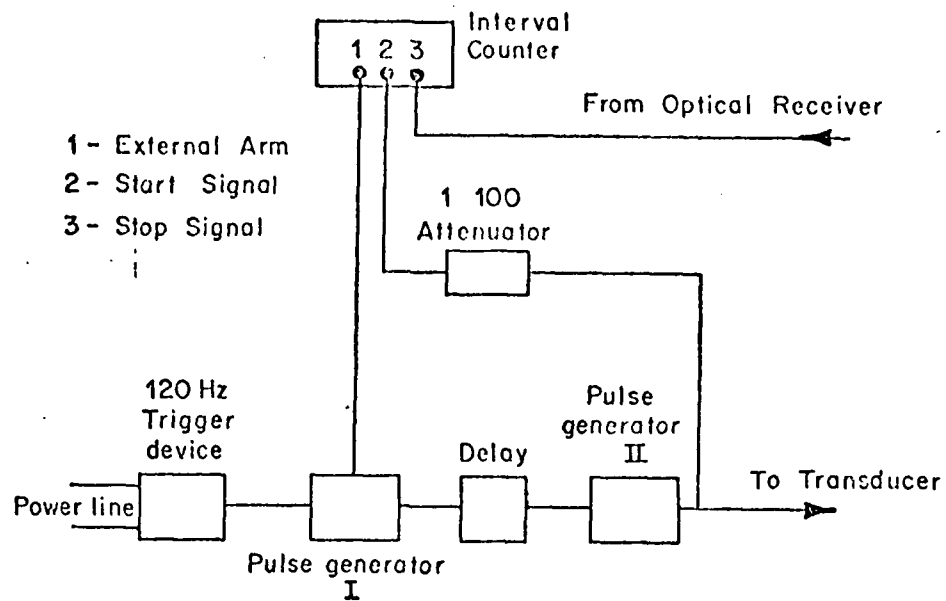


Fig. 8 Schematic of timing control system.

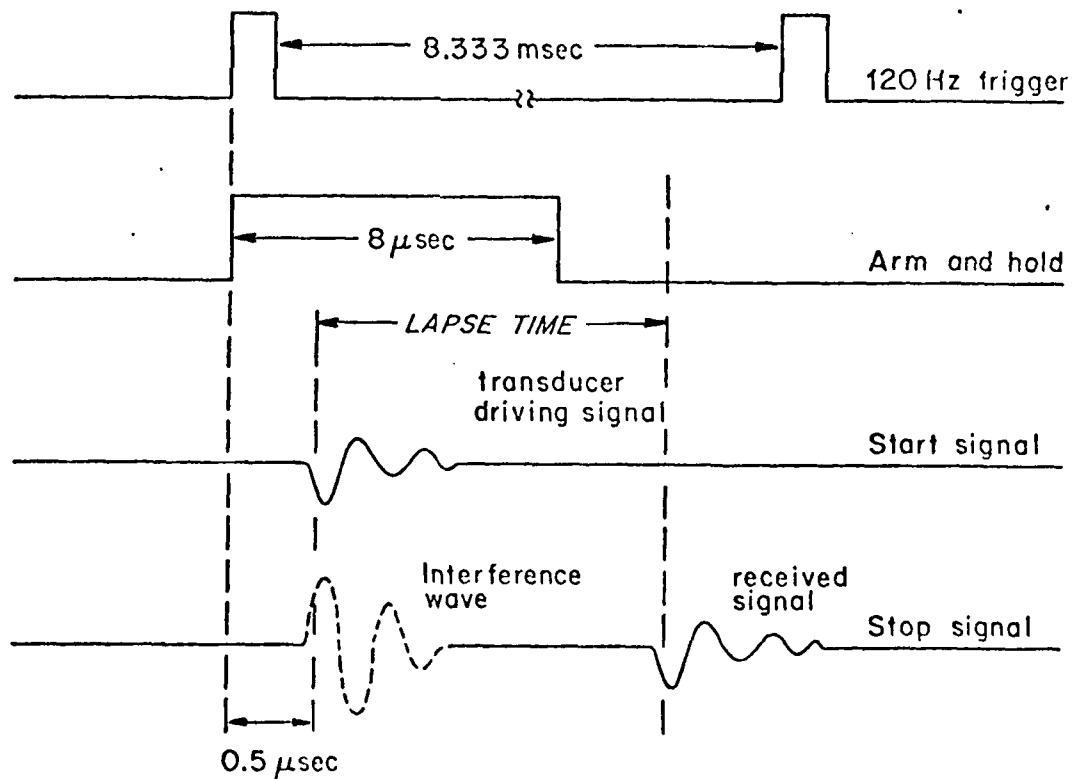


Fig. 9 Schematic of timing sequence.

that even with low repetition rates which eliminated the reverberation affect the received acoustic pulse still exhibited an amplitude jitter of about 3%, which caused significant timing errors. This jitter was traced back to a systematic laser intensity fluctuation of about 3% with a period of 360 cycles (related to the line frequency), which was caused by the laser intensity control system. The effect of this systematic laser intensity fluctuation can be avoided if the timing is such that the laser has the same intensity whenever the acoustic pulse is picked up by the optical detection system. This is the case if the repetition rate of the measurement sequence is a subharmonic of the fluctuation frequency. A 120 Hz repetition rate pulse generator with the timing derived from the line voltage was used in our system. This scheme removed the effect of the systematic laser intensity fluctuations. The remaining random fluctuations were insignificant. This master pulse generator triggered pulse generator I to emit an 8 μ sec pulse which was supplied to the arm and hold terminal of the interval counter. This activates the interval counter in such a way that a subsequent start event (supplied to the "start" terminal of the counter) initiates the counting, but inactivates the counter for all "stop" events (supplied to the stop terminal of the counter) for the (8 μ sec) duration of the arm and hold pulse. The same 8 μ sec pulse is delayed by .3 μ sec and then triggers the high voltage pulse-generator II, to emit a 600 volt 40 n sec pulse which activates the piezoelectric transducer, and launches the acoustic pulse into the test sample. The same pulse appropriately attenuated is

supplied to the start terminal of the counter. Finally the photoreceiver output connected to the stop terminal of the counter, provides the stop signal to the interval counter. Ideally the stop signal is provided by the optically picked up acoustic pulse after it traversed the test sample. However the transducer assembly when activated by the high voltage pulse emits an electromagnetic interference signal which is picked up by the photoreceiver and transmitted to the counter as an unwanted stop signal. The counter operating in the arm and hold mode however ignores any stop signal during the 8 μ sec hold period, but is ready to respond to the desired stop signal which (in our experiments) appears about 8.7 μ sec after the acoustic pulse has been launched into the test object.

A diagram of the timing sequence is shown in Fig. 9.

Section 3

Timing accuracy.

The timing errors inherent in the measurement system described above has systematic and random components, which are due partly to inherent limitation of the interval counter and partly to other system characteristics. The interval counter according to the specifications has a systematic error of ± 700 ps. which is the largest single error component. This error however is irrelevant for relative lapse time measurements taken with virtually unchanged instrument settings and input characteristics, and will therefore not be considered further. The timing errors of significance are the random errors which are due to the instrument jitter, the noise characteristics of the stop signal

supplied to the counter, and a removable systematic error which in our system is due to the finite size of the acoustic transducer. We shall in the following discuss this three error components and compare in Section 4 the theoretical predictions with experimental results.

We consider first the random RMS timing error e . It is given by:

$$e = \text{instrument jitter} + e_t / \sqrt{N} \quad (12)$$

The instrument jitter is according to instrument specification typically ± 35 psec and is independent of N . N is the number of individual time measurements over which the instrument averages to display one data point, e_t is the trigger error. It depends on the RMS noise voltage V_n and the slew rate of the stop signal at the trigger point:

$$e_t = V_n / \text{slew rate} . \quad (13)$$

The stop signal in our case is the photodetector output pulse, which is essentially a damped sinusoidal pulse with a nominal frequency of $\nu = 5$ MHz, a peak voltage of around $V_{\max} = .5$ volts and an RMS noise of about $V_n = 3.5$ mV. For reasons to be discussed later the trigger point was chosen at the first zero crossing of the pulse waveform. The slew rate at this trigger point is given by $2\pi\nu V_{\max} = 16$ V/ μ sec. This gives for the trigger error $e_t = 220$ psec.

In our experiments we averaged typically over $N = 100$, sometimes over $N = 1000$ individual measurements. The residual expected RMS error e in the displayed mean values is therefore:

$$\begin{aligned} e &= 55 \text{ psec for } N = 100 \\ e &= 42 \text{ psec for } N = 10^3 \end{aligned} \quad (14)$$

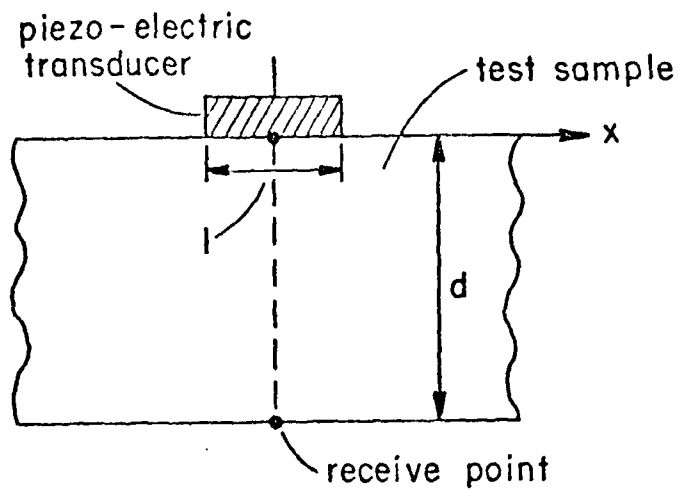


Fig. 10 Schematic of measurement geometry
receiver centered
underneath transducer.

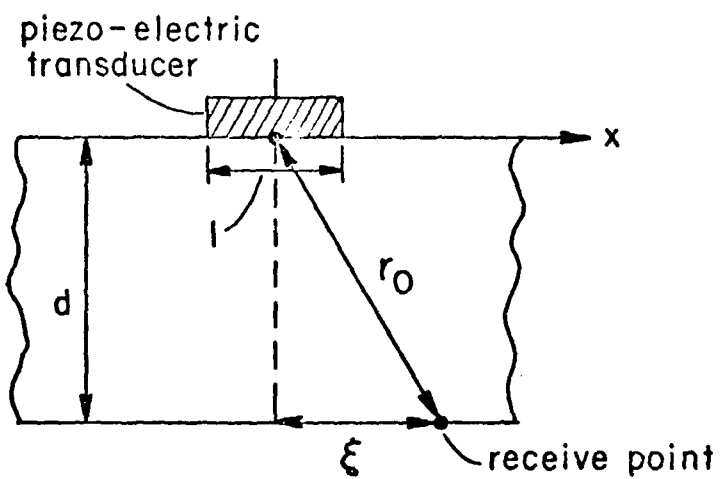


Fig. 11 Schematic of measurement geometry
Fixed transducer,
moving receiver.

The most important systematic error in the lapse time measurement scheme described here, which employs piezoelectric transducers as acoustic emitter, and a laser beam as acoustic receiver is caused by the finite size of the transmitting transducers. The measurement geometry typically employed is shown schematically in Fig. 10. The objective is to measure the transit time of an acoustic pulse launched into the test object by the piezoelectric transducer and picked up by a "point receiver" represented by the laser beam. The test object is a steel block of thickness d . We consider first the "simple" case that the receive point lies underneath the center of the transmitting transducer.

The problem which arises in this measurement situation is to define what is meant by "pulse transit time". In the ideal case that both transmitter and receiver are "point" transducers, any pulse excitation $f(t)$ beginning at $t = 0$ at the transmitter would be picked up by the receiver as a delayed copy $F(t)$ of the excitation pulse:

$$F(t) = f(t - \frac{d}{c}) \quad (16)$$

In this case the delay time $\Delta t = d/c$ clearly defines the transit or lapse time. If the pulse has a sharp rising edge at $t=0$, the obvious measurement strategy would be to determine the arrival time of the leading edge of the pulse at the receiver, i.e., to use this leading edge as trigger point to stop the interval counter.

However if the same pulse excitation $f(t)$ is applied to a finite area transducer, every surface element underneath the

transducer acts like a point transmitter, and the received signal $F(t)$ is the sum of the excitation from all points of the excited surface each with its own delay r/c :

$$F(t) \propto \int_A f(t - \frac{r}{c}) df \quad (17)$$

where A is the area under the transducer, df the surface element and r the distance from a particular surface element to the receive transducer. Introducing a cartesian coordinate system (x,y) with its origin at the center of the transducer, r becomes:

$$r = \sqrt{d^2 + x^2 + y^2} \approx d + \frac{x^2}{2d} + \frac{y^2}{2d} . \quad (18)$$

The second approximate eq. (18) is valid for transducers with linear dimensions small compared to d .

With the received signal $F(t)$ given by eq. (17) the clear cut concept of a pulse transit time is lost and the strategy to use the leading edge of $F(t)$ as the trigger point to stop the interval counter, is not possible because, even for a steep leading edge of $f(t)$ the leading edge of $F(t)$ is soft with a zero slope at $\Delta t = d/c$, giving rise to an unacceptably large trigger error. This makes it necessary to devise a workable strategy for the case at hand. To do this we have to analyze the received function $F(t)$ for the excitation pulse shape used in our experiments.

We have mentioned earlier that because of the ringing of the transducer the excitation pulse is a damped sinusoid. To simplify our analysis we model this pulse by an undamped sinusoid of finite duration. Since, as we shall see presently, our time

measurement is completed after the first zero-crossing of $F(t)$, neglectation of the damping has only a minor effect, and furthermore the pulse duration does not enter our considerations. We can therefore model our pulse $f(t)$ by:

$$f(t) = \sin(\omega t) \cdot \theta(t) \quad (19)$$

where θ is the discontinuous factor:

$$\theta = \begin{cases} 0 & \text{for } t < 0 \\ 1 & \text{for } t > 0 \end{cases} \quad (20)$$

With this excitation the received signal eq. (17) becomes

$$F(t) \propto \int_{-l/2}^{+l/2} \int_{-l/2}^{+l/2} \sin\omega(t - \frac{d}{c} - \frac{x^2}{2dc} - \frac{y^2}{2dc}) \cdot \theta(t - \frac{r}{c}) dx dy \quad (21)$$

The limits on the double integral are for a square transducer with linear dimension l .

The function $F(t)$ defined by (21) is zero for $t < d/c$ and increases slowly with zero slope for $t > d/c$, until all the contributions from the excited area under the transducer have arrived.

This happens at the time:

$$t = \frac{r_{\max}}{c} = \frac{d}{c} (1 + \frac{l^2}{4dc}) \quad (22)$$

From this time on $F(t)$ continues as a sine wave:

$$F(t) \propto \sin\{\omega(t - \frac{d}{c}) - \phi(l)\} , \quad \text{for } t > \frac{r_{\max}}{c} \quad (23)$$

with a phase shift $\phi(l)$ relative to the phase $\omega(t - \frac{d}{c})$ of the received signal for the ideal case of a point transducer.

Provided that the time interval:

$$\Delta t = \frac{r_{\max} - d}{c} , \quad (24)$$

during which contribution to $F(t)$ still arrive at the receive point, is small compared to the period $T = \frac{2\pi}{\omega}$ of the excitation signal, (which is always the case in the experiments to be described later) the slope of $F(t)$ has an absolute maximum at:

$$t = d/c + \frac{\pi}{2\omega} + \frac{\phi(\ell)}{\omega} \quad (25)$$

which as follows from eq. (23) is the first zero-crossing of $F(t)$. This point is an obvious choice for the trigger point, that is the point at which the interval counter, stops counting. The reasons for this choice are threefold. First the positions in time of the first zero crossing is independent of the amplitude of $F(t)$. Secondly since $F(t)$ has its highest slope at this point the trigger error, as we have seen above, is minimized and thirdly the observed lapse time:

$$t_{\ell} = d/c + \frac{\pi + \phi(\ell)}{\omega} \quad (26)$$

has a well defined relationship to the actual parameter of interest, the transit time of the leading edge of a pulse for the ideal case of a point transmitter and point receiver:

$$t_{\ell 0} = d/c . \quad (27)$$

We can now proceed to calculate this phase shift $\phi(\ell)$.

Because of eq. (20) the function $\theta(t - r/c)$ is unity for $t > \frac{r_{\max}}{c}$ and $F(t)$ eq. (21) becomes:

$$F(t) \propto \int_{-\ell/2}^{\ell/2} \int_{-\ell/2}^{\ell/2} \sin \omega \left(t - \frac{d}{c} - \frac{x^2}{2cd} - \frac{y^2}{2cd} \right) dx dy \quad (28)$$

Eq. (28) can be rewritten as:

$$F(t) \propto \text{Im}\{e^{i\omega(t-d/c)} \left(\int_{-l}^{+l} e^{-\frac{i\omega u^2}{2dc}} du \right)^2\} \quad (29)$$

where $\text{Im}\{ \}$ indicates the imaginary part of the function inside the brackett. Letting:

$$I_1 = \int_{-l/2}^{+l/2} \cos \frac{\omega u^2}{2dc} du \text{ and } I_2 = \int_{-l/2}^{+l/2} \sin \frac{\omega u^2}{2dc} du, \quad (30)$$

$F(t)$ becomes

$$F(t) \propto (I_1^2 + I_2^2)^2 \text{Im}\{e^{i\omega(t-d/c)-2\phi(l)}\}$$

with

$$\phi(l) = \text{tg}^{-1}(I_2/I_1) \quad (31)$$

Neglecting as inmaterial the time independent amplitude factor we finally obtain for $F(t)$:

$$F(t) \propto \sin\{\omega(t - \frac{d}{c}) - 2\phi(l)\} \quad (32)$$

This phase delay translates into a time delay $\Delta t = \frac{\phi(l)}{\omega}$.

Placing the trigger point at the first zero crossing of $F(t)$ therefore results in a measured lapse time which is related to the acoustic time of flight between the centerpoint of the transmitter and the receive point by

$$\text{Time of flight} = \text{Lapse time} - \frac{\pi}{\omega} - \frac{2\phi(l)}{\omega} \quad (33)$$

For a 5 cm thick steel block and transducer dimensions of $l = 4$ mm and $l = 8$ mm respectively and a frequency of 5 MHz one finds for $2\phi(l)$:

$$2\phi(l) = .143 \text{ rad}$$

$$\Delta t = 4.566 \text{ n sec}$$

$$2\phi(l) = .498 \text{ rad}$$

$$\Delta t = 15.867 \text{ n sec}$$

This corrections are non trivial for lapse time measurement accuracies of 50-100 p sec which as we have seen above are obtainable with the described measurement system.

We can now treat in complete analogy to the foregoing analysis the more interesting case where the receiver laser beam is scanned over the object surface on a straight line passing through the projection of the transducer center, for which we just calculated the time corrections. This situation is shown schematically in Fig. 11. Referring to Fig. 11 we characterize the laser spot position on its scanning line by the variable ξ . We assume without loss of generality, that the scanning line on the receiver surface of the object runs parallel to the x-axis of the coordinate system on the transducer surface defined above. The distance from the transducer center to the receiver point ξ is then:

$$r_o = \sqrt{d^2 + \xi^2} . \quad (34)$$

The distance r from an arbitrary point at the transducer surface to the receiver point is:

$$r = \sqrt{d^2 + (\xi-x)^2 + y^2} = \sqrt{r_o^2 - \xi^2 + (\xi-x)^2 + y^2} \quad (35)$$

which, with the same approximation as above reduces to:

$$r = r_o - \frac{\xi^2}{2r_o} + \frac{(\xi-x)^2}{2r_o} + \frac{y^2}{2r_o} , \quad (36)$$

and we find again for $F(t)$:

$$F(t) \propto I_m \{ e^{i\omega(t-r_0/c) + i\omega\xi^2/2r_0c + \ell/2} \int_{-\ell/2}^{\ell/2} e^{-i\frac{\omega(\xi-x)^2}{2r_0c}} dx + \int_{-\ell/2}^{\ell/2} e^{-i\frac{\omega y^2}{2rc}} dy \}$$

$$\text{for } ct > \sqrt{d^2 + (\xi + \ell/2)^2 + (\ell/2)^2}$$

and therefore

$$F(t) \propto \sin\{\omega(t - \frac{r_0}{c}) + \phi(\xi) - \phi(\xi, \ell) - \phi(\ell)\} \quad (38)$$

with

$$\phi(\xi) = \frac{\omega\xi^2}{2r_0c}.$$

$$\phi(\xi, \ell) = \text{tg}^{-1} \left\{ \frac{\ell/2 - \xi}{-\ell/2 - \xi} \int_{-\ell/2 - \xi}^{\ell/2 - \xi} \sin\left(\frac{\omega u^2}{2rc}\right) du / \int_{-\ell/2 - \xi}^{\ell/2 - \xi} \cos\left(\frac{\omega u^2}{2rc}\right) du \right\} \quad (39)$$

$$\phi(\ell) = \text{tg}^{-1} \left\{ \frac{\ell/2}{-\ell/2} \int_{-\ell/2}^{\ell/2} \sin\left(\frac{\omega u^2}{2rc}\right) du / \int_{-\ell/2}^{\ell/2} \cos\left(\frac{\omega u^2}{2rc}\right) du \right\}$$

For $\xi=0$, r_0 reduces to d , $\phi(\xi)$ goes to zero and $\phi(\xi, \ell)$ goes to $\phi(\ell)$, and therefore $F(t)$ becomes again:

$$F(t) \propto \sin\{\omega(t-d/c) - 2\phi(\ell)\}$$

the same as in eq. (31) which we derived for the special case $\xi=0$ above. Here again we chose as trigger point the first zero crossing of $F(t)$. The reduction of the measured lapse time to the desired flight time from the transducer center to the receive point now requires three correction terms:

$$\text{Time of flight} = \text{Lapse time} - \frac{\pi}{\omega} + \frac{\phi(\xi)}{\omega} - \frac{\phi(\xi, \ell)}{\omega} - \frac{\phi(\ell)}{\omega} \quad (40)$$

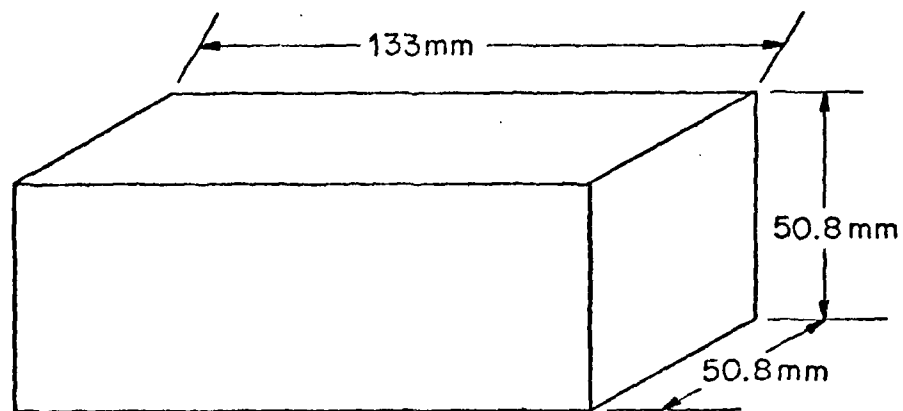


Fig. 12 Test sample for group I experiments.

Section 4. Experimental Results.

The experiments which were performed with the completed measurement system fell into two groups. The first group was designed to establish experimentally the accuracy of the system. The second group were measurements on a sample with artificially introduced residual strain.

Group I Experiments.

The accuracy test were performed on a homogeneous nominally stress free steel block with dimensions shown in Fig. 12. The experiment geometry is that of Fig. 11. One long side faces of the steel block was polished. This polished face was used as the receiver side of the block. The other three side faces were machine ground. We used two different transducers to launch the acoustic pulse into the sample. Transducer one was a square transducer with $\ell=4$ mm. Its ringing frequency was 3.95 MHz. The second transducer was also square with a side dimension of $\ell=8$ mm its ringing frequency was slightly smaller (3.2 MHz).

The first measurement was made with the receiver spot opposite to the transducer center (see Fig. 10). The observed lapse time with transducer 1 was: $t_{\ell_1} = 8.655300$ with transducer two $t_{\ell_2} = 8.702220$.

Using the corrections formula eq. (33) gives for the corrected time of flight for the two measurements:

$$t_{f_2} = 8523.350 \pm 80 \text{ psec,}$$

$$t_{f_2} = 8523.440 \pm 80 \text{ psec.}$$

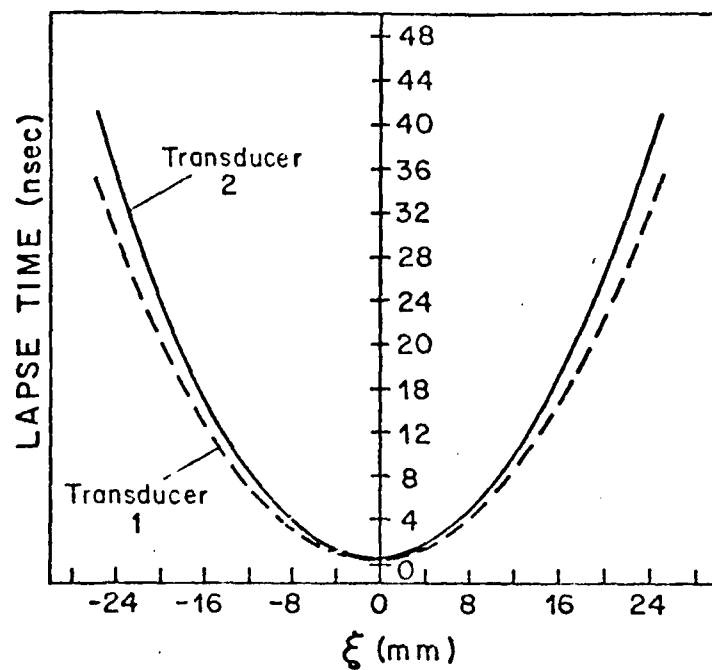


Fig. 13 Lapse time for two different transducers.

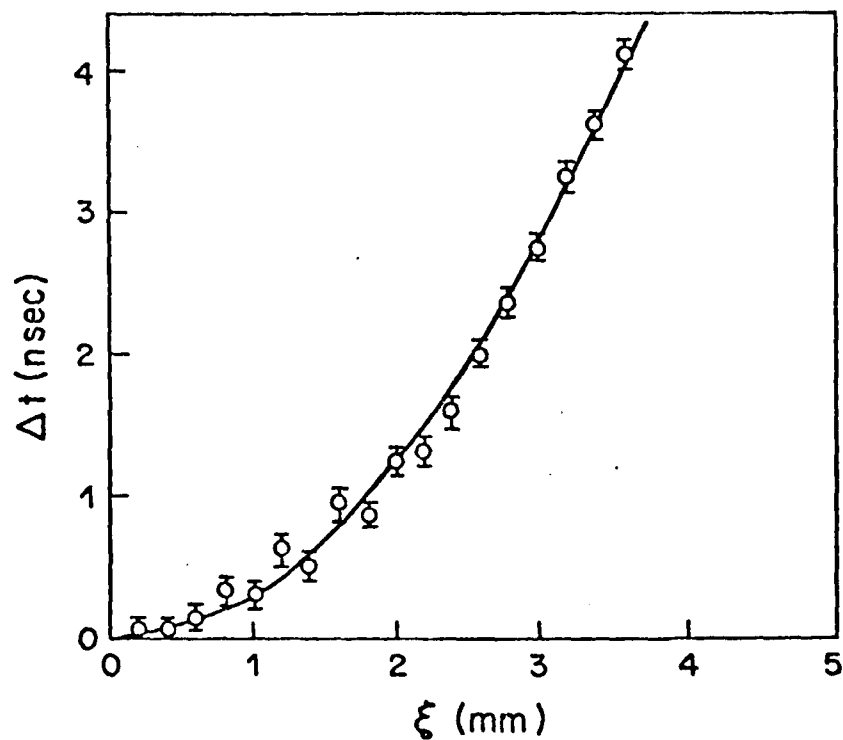


Fig. 14 Lapse time difference theoretical & experimental.

The two measurements agree within the expected accuracy. This does not imply however that we can measure absolute velocity to the same accuracy since the counter has a systematic error of ± 1 n sec which as we pointed out above is irrelevant for relative time measurements. Taking this error into account we find for the velocity in our steel block:

$$5.960 \pm 6 \cdot 10^{-4} \text{ m/sec.}$$

Holding the transducer stationary and moving the receiver light spot across the sample (see Fig. 11) we obtained for the two transducers two slightly different parabolic lapse-time responses which are shown in Fig. (13). The laps time difference of 47.055 nsec at $\xi=0$ is not shown in Fig. (13) since the feature of interest is the change in lapse time observed with the two transducers as ξ increases:

$$\Delta t(\xi) = \frac{\phi_1(\ell_1 \xi)}{\omega_1} - \frac{\phi_2(\ell_2 \xi)}{\omega_2}$$

where ϕ_1 is the phase correction eq. (40) for transducer "1" with length ℓ_1 and frequency ω_1 and ϕ_2 the corresponding phase correction for transducer "2" with length ℓ_2 and frequency ω_2 .

This lapse time dependence on the receiver excursion ξ with parameter values:

$$d = 50.8 \text{ mm, } c = 5.96 \cdot 10^3 \text{ m/sec}$$

$$\ell_1 = 2 \text{ mm} \quad \omega_1 = 3.95 \text{ MHz} \quad \ell_2 = 8 \text{ mm} \quad \omega_2 = 3.2 \text{ MHz}$$

is shown in Fig. 14. Also shown in Fig. 14 are the experimentally observed time differences with their expected error. Fig. 14 shows that the experimental data agree within the expected error

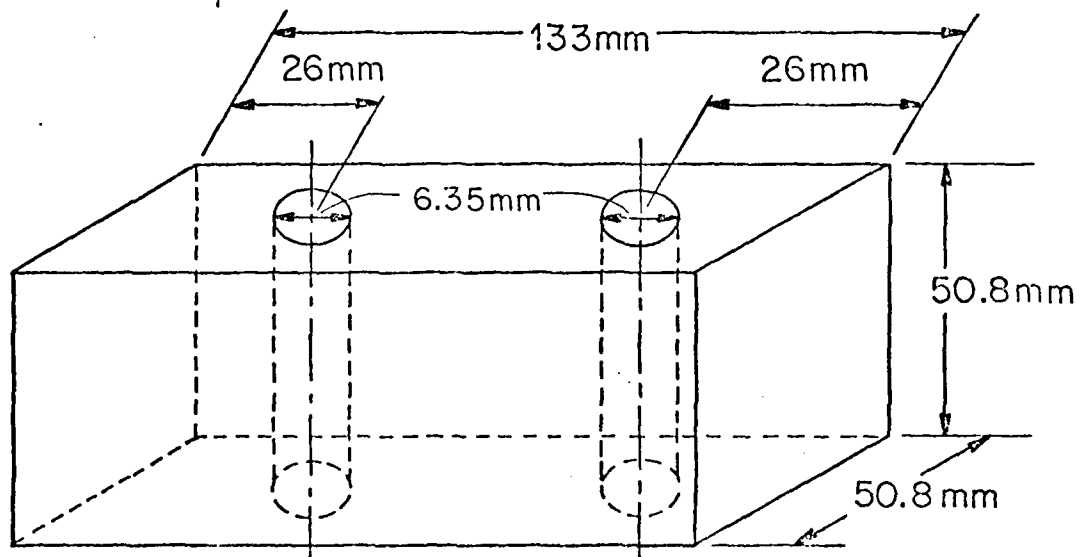


Fig. 15 Test sample for group II experiments.

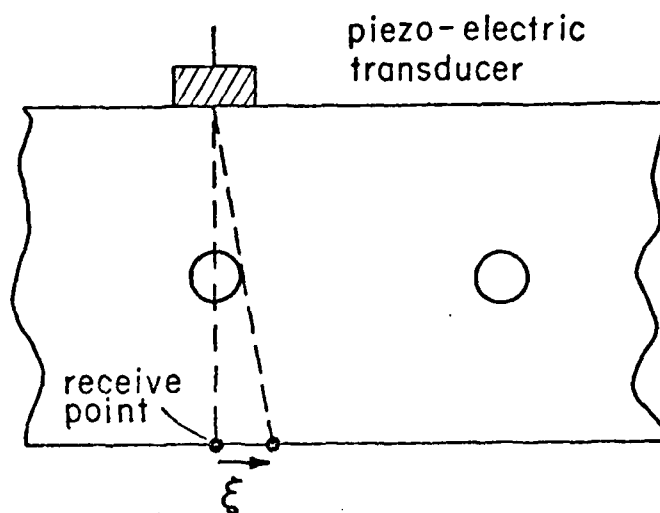


Fig. 16 Measurement geometry for first set of group II experiments.

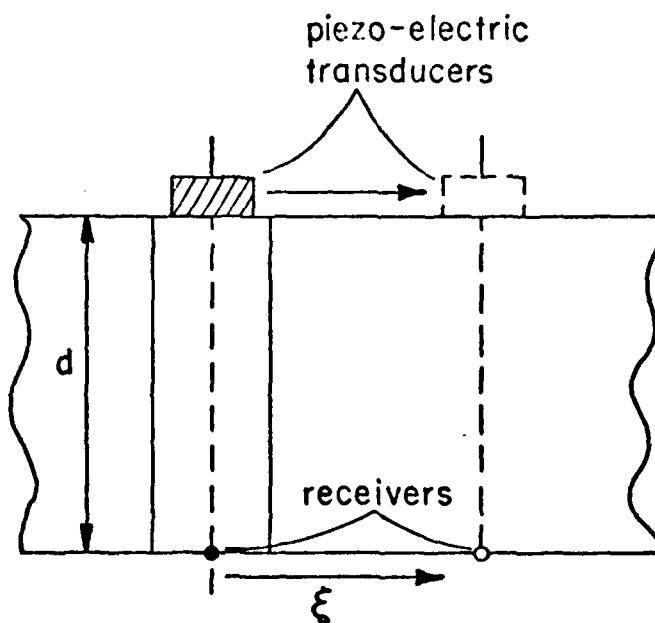


Fig. 19 Measurement geometry for second set of group II experiment.

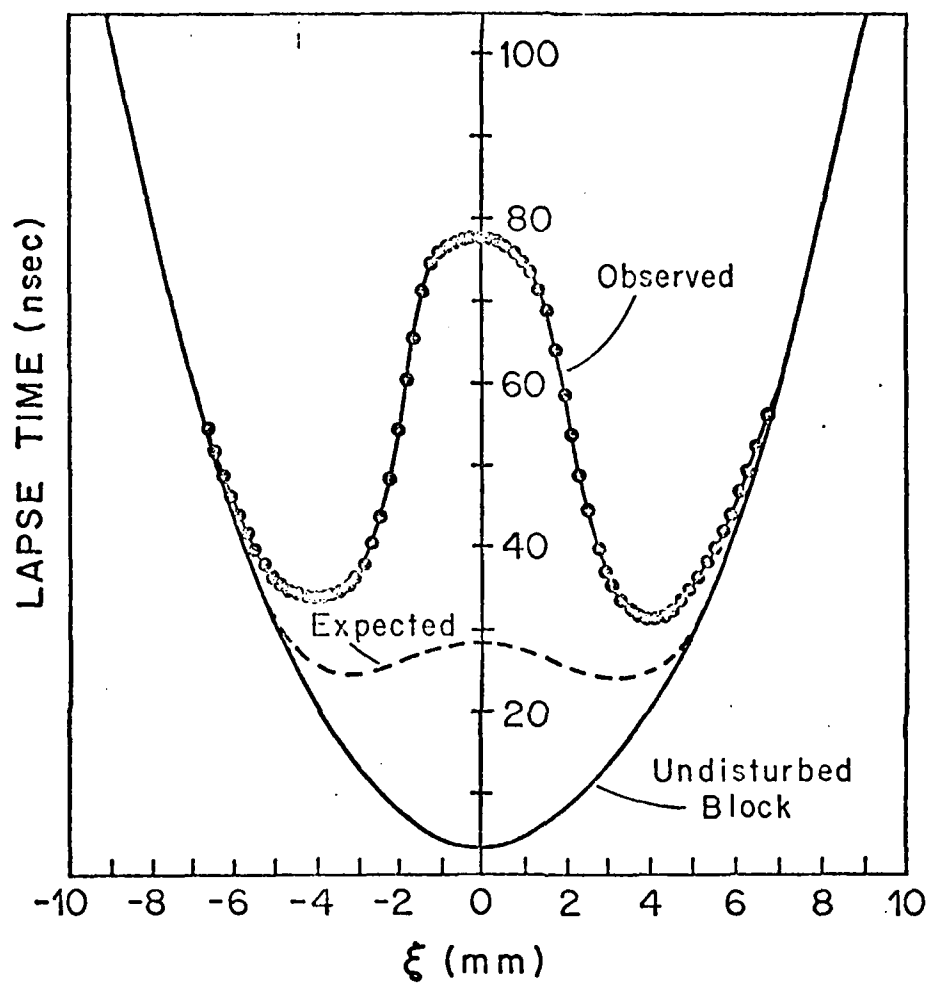


Fig. 17 Observed lapse time in test sample with stainless steel pin. Sound propagating perpendicular to pin axis.

The geometry for the first set of measurements is shown in Fig. 16. The transducer was in a fixed position over the axis of the rod and the receive spot was moved along a line perpendicular to the rod axis. In Fig. (17) the results for the stainless steel rod are shown. Curve 1 is the measured lapse time. For comparison curve 2 shows the lapse time for the homogeneous block observed in the group 1 experiments, and curve three shows the expected response due to the presence of the stainless steel rod, calculated under the assumption that the boundary between rod and matrix is acoustically transparent.

Surprisingly the lapse time difference due to the presence of the stainless steel pin is much greater than the effect which can be caused by the 3% velocity difference between rod and matrix material. The larger observed time difference can be explained however if one assumes that the boundary between rod and matrix is highly reflective and not as we expected transparent to sound. An independent indication for the high reflection coefficient of the boundary was the severely reduced amplitude of the received signal in the shadow zone of the rod. If one assumes total reflection at the rod, the only sound which can reach the geometric shadow zone, is the sound scattered around the obstructing pin. This sound arrives with a delay Δt relative to the direct signal in the homogeneous matrix, given by:

$$\Delta t = 2 \frac{\sqrt{(d/2)^2 - r^2} - d/2}{c_0} .$$

For the parameters in our experiment this gives

$$\Delta t = 73 \text{ n sec.}$$

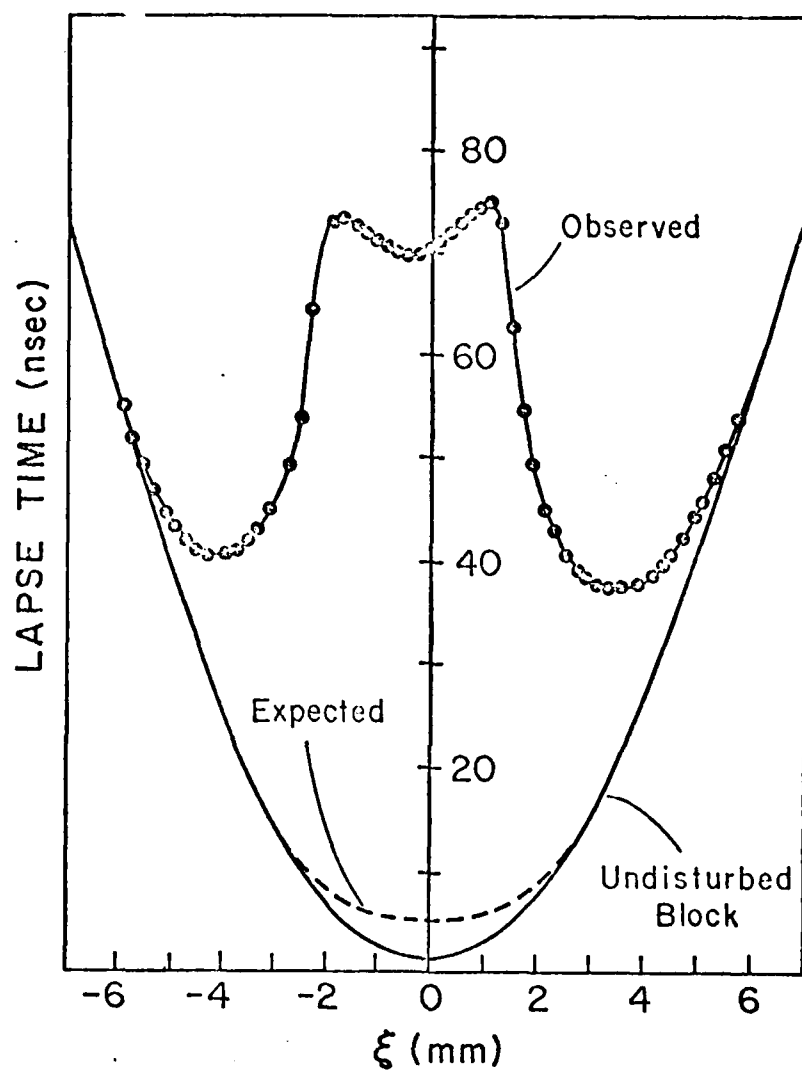


Fig. 18 Observed lapse time in test sample with mild steel pin. Sound propagating perpendicular to pin axis.

This delay compares very well with the observed delay of 75 n sec shown in Fig. (17).

We have no good explanation for this apparent high reflectivity of the boundary zone, but as we shall see additional evidence for its existence.

In Fig. (18) the results of lapse time measurements using the mild steel rod in the same geometry are shown. The compressional stress in the rod should have reduced the velocity by about .5% giving rise to the expected lapse time shown in curve 2 of Fig. 18 but again we see a much larger effect which we can account for by invoking the high reflection at the boundary. In addition we see at the edge of the rod (at ± 3 mm) a structure in the lapse time which appears to reflect, although diminished by the shadow effect, the velocity distribution inside the rod. This velocity distribution is observed directly with a measurement geometry shown in Fig. (19). In this case the acoustic propagation vector is parallel to the rod axis and both, transducer and receive point move together in such a way that the receive point stays in line with the center of the transducer. The resulting lapse time is shown in Fig. (20). Zero lapse time in Figs. (20) and (21) represent the lapse time one would obtain for the homogeneous block. The measured lapse time again differs substantially from the lapse time shown in Fig. 21 which would result from the "design" stress field discussed above. Let us consider first the expected lapse time Fig. (21). It is shown in the literature [7] that the longitudinal wave velocity in stressed material propagating along the direction of one of the principal stress (or

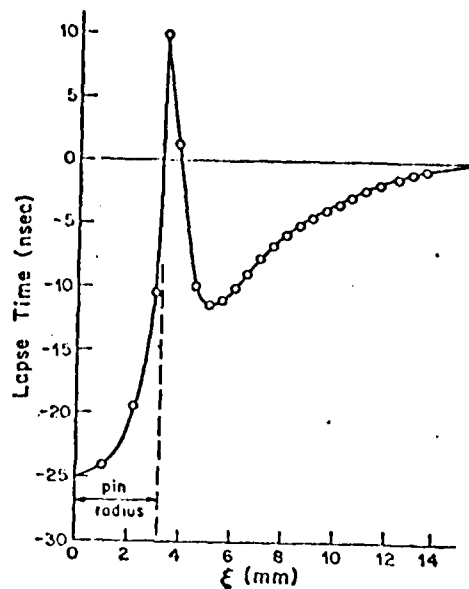


Fig. 20 Observed lapse time in test sample with mild steel pin. Sound propagating parallel to pin axis.

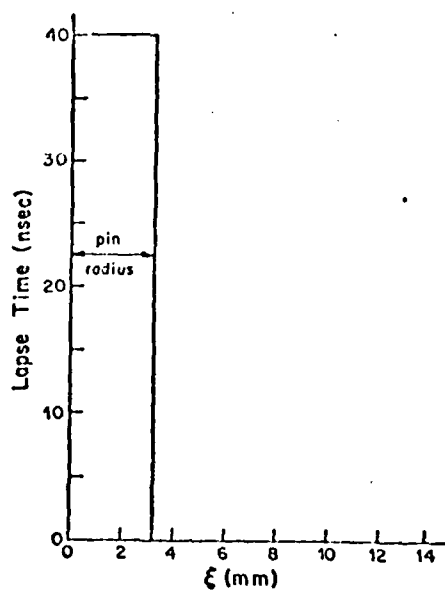
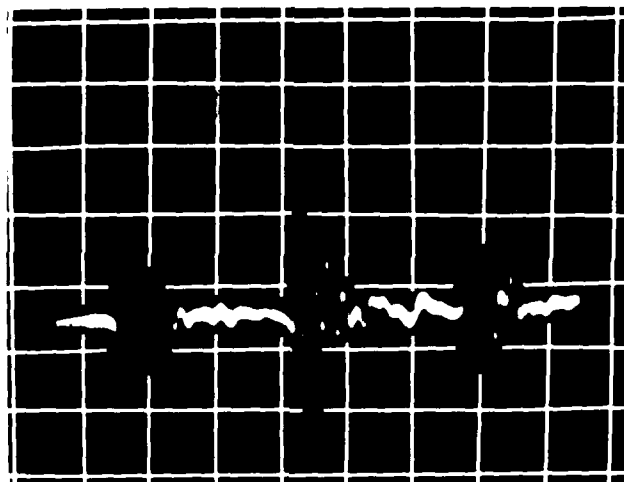


Fig. 21 Expected lapse time with measurement geometry of Fig. 19.

a)



b)

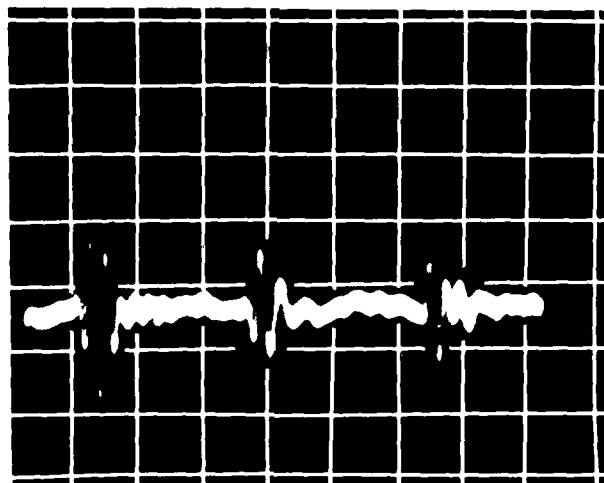


Figure 22 : a) Direct pulse train observed in measurement configuration shown in Fig. 19. Time scale , $0.5 \mu\text{sec} / \text{cm}$. Voltage scale , $50\text{mV} / \text{cm}$.
b) Doubly reflected pulse train. Time scale, $0.5 \mu\text{sec} / \text{cm}$. Voltage scale, $20\text{mV} / \text{cm}$.

strain) axes depends only on the dilatation and the principal strain component parallel to the propagation vector. Our "design" stress field in the matrix outside the rod has two non zero principal strain components, radial compression and angular tension of equal magnitude, resulting in zero dilatation. Therefore the velocity parallel to the rod axis is not affected by this stress field. In the pin on the other hand there exists only radial compression, resulting in a net negative dilatation (Volume compression) which decreases the sound velocity by an expected .4%.

The actual measurement shows in contrast an increase of the velocity inside the pin by about .28%. Unfortunately we did not measure the sound velocity in the pin before it was inserted into the block. It is therefore possible that this small deviation in velocity from the matrix material indicated by Fig. (20) is due to a combination of stress and material differences, so that no conclusion can be drawn regarding the stress field in the pin. The observed lapse time inside the pin however corroborates our interpretation of Fig. 18. The observed smaller lapse time in the matrix outside the pin, on the other hand clearly represents increased velocity (to .13% at maximum) which indicates a radially decaying tensile stress component along the axis of the pin probably caused by strong shear stresses in the boundary. The peak at the boundary furthermore indicates a strong boundary disturbance, which most likely is related to the observed but not understood boundary behavior.

With the measurement geometry shown in Fig. 19 we observed with both rods an interesting acoustic phenomenon which we report here without an attempt toward its explanation.

With transmitter and receiver inside the pin area, and only in this configuration, the received pulse had two satellites which were essentially replicas of the main pulse but delayed by 1.6 and 3.5 μ sec respectively. An oscilloscope trace of this three pulses is shown in Fig. (22a). The tentative explanation that the rods isolated by their reflective boundaries might support guided waves with different propagation velocities, was ruled out by an other observation. Due to the small attenuation of ultrasound in steel we could observe the same pulse train after it was reflected first on the receiver face of the block and than at the transducer face, returning to be picked up again by the receiving laser beam. This doubly reflected pulse train is shown in Fig. 22b. Fig. 22b shows that the relative arrival times of the three pulses are unchanged. This clearly rules out the possibility that the pulses travel with different velocities. This phenomenon was never observed with the transducer, the receiver, or both outside the rod area.

Conclusion

In the course of this work we have designed and built an experimental acousto-optic time of flight measurement system, and demonstrated a timing accuracy of ± 80 psec. The timing accuracy was demonstrated by measuring lapse time changes caused by small but well defined pathlength changes in the test object.

We also intended to relate quantitatively lapse time measurements to residual stresses in a test sample with a known residual stress distribution. However substantially different velocity changes than those predicted from the "design" stresses were

With transmitter and receiver inside the pin area, and only in this configuration, the received pulse had two satellites which were essentially replicas of the main pulse but delayed by 1.6 and 3.5 μ sec respectively. An oscilloscope trace of this three pulses is shown in Fig. (22a). The tentative explanation that the rods isolated by their reflective boundaries might support guided waves with different propagation velocities, was ruled out by an other observation. Due to the small attenuation of ultrasound in steel we could observe the same pulse train after it was reflected first on the receiver face of the block and than at the transducer face, returning to be picked up again by the receiving laser beam. This doubly reflected pulse train is shown in Fig. 22b. Fig. 22b shows that the relative arrival times of the three pulses are unchanged. This clearly rules out the possibility that the pulses travel with different velocities. This phenomenon was never observed with the transducer, the receiver, or both outside the rod area.

Conclusion

In the course of this work we have designed and built an experimental acousto-optic time of flight measurement system, and demonstrated a timing accuracy of ± 80 psec. The timing accuracy was demonstrated by measuring lapse time changes caused by small but well defied pathlength changes in the test object.

We also intended to relate quantitatively lapse time measurements to residual stresses in a test sample with a known residual stress distribution. However substantially different velocity changes than those predicted from the "design" stresses were

observed. This defeated our original purpose, but served to demonstrate that the system is capable to detect and quantize residual stresses.

With the demonstrated accuracy stress detection with longitudinal acoustic waves becomes a practical possibility. Data in the literature [8] indicate that stresses of the order of 10^3 psi cause longitudinal wave velocity changes of about .1% in steel. Assuming a one inch measurement base this corresponds to an acoustic time of flight change of $\Delta t = 4$ nsec. This is 50 times the minimum observable lapse time change of the present system.

References

1. P. J. Noronha and J. J. West, British Journal of NDT, Sept. 1969.
2. B. P. Hildebrandt and T. P. Harrington, Butelle N.W. Report #23112 03073, (1978).
3. B. P. Hildebrandt and D. E. Huffard, Acoustical Holography Vol. 7, p. 245, Plenum Press, 1977.
4. R. von Gutfeld and H. Budd, Appl. Phys. Letters, Vol. 34, p. 617 (1979).
5. John Gosh, Electronics, January 1982.
6. A. Korpel, Acoustical Holography, Vol. 1, p. 149, Plenum Press, 1969.
7. R. K. Mueller and R. Rylander, J. Opt. Soc. Am., Vol. 69, p. 182 (1979).
8. C. Tynesdell and W. Noll, Handbach der Physik, Vol. III/3, p. 288, Springer Berlin-New York, 1965.
9. D. I. Crecruft, Ultrasonics, Vol. 6, p. 207 (1968).